Rapid Communications

Pressure-induced disruption of the local environment of Fe-Fe dimers in $FeGa_3$ accompanied by metallization

G. R. Hearne,* S. Bhattacharjee, B. P. Doyle, M. A. M. Ahmed, P. Musyimi, and E. Carleschi
Department of Physics, University of Johannesburg, P.O. Box 524, Auckland Park 2006, Johannesburg, South Africa

B. Joseph
Elettra, Sincrotrone Trieste, Strada Statale 14, Km 163.5, Basovizza, 34149 Trieste, Italy

(Received 17 April 2018; revised manuscript received 15 June 2018; published 23 July 2018)

The semiconducting gap in the $FeGa_3$ intermetallic originates from Fe($3d$)/Ga($4p$) hybridization. Pressures of 15–20 GPa initiate a disruption of this semiconducting tetragonal $P4_2/mnm$ structure and an emergence of a high-pressure metallic phase, estimated to be fully stabilized just beyond ∼35 GPa. An accompanying pronounced ∼17% volume collapse occurs at the structural transition. The high-pressure metallic phase has a $T^{1/2}$ temperature dependence of the resistivity below its minimum at 8–12 K, symptomatic of disorder. There is a corresponding weak high-temperature dependence of the resistivity and resultant broad maximum at ∼250 K to yield "bad-metal" values of ∼0.5 mΩ cm at room temperature. This is shown to signify that the high-pressure phase is a low carrier density metal on the verge of an Anderson transition. Ga K-edge absorption spectroscopy and Fe Mössbauer spectroscopy local probes indicate that the atomic disorder stems from a pressure-instigated rearrangement of the Ga sublattice at the structural transition.

DOI: 10.1103/PhysRevB.98.020101

Introduction. First-principles electronic structure calculations show a narrow charge gap formation (300–500 meV) in the $FeGa_3$ intermetallic that originates from strong hybridization between Fe $3d$ and Ga $4p$ orbitals [1–5], analogous to other hybridization-gapped systems $FeSb_2$ and FeSi. The narrow gap opening is reminiscent of that originating from $4f$ levels hybridizing with broader transition-metal conduction bands in Kondo systems [6]. This similarity has invoked considerable interest in the above-mentioned systems as $3d$ analogs of such Kondo semiconducting states [6–8].

Additionally, $FeGa_3$ has been extensively studied as a thermoelectric material. Narrow peaks in the electronic density of states below and above the band gap are considered favorable for these enhanced thermoelectric properties [1,4,5]. Exceedingly large negative values of the Seebeck coefficient (of a few hundred $\mu V\,K^{-1}$) have been measured at room temperature (RT) in polycrystalline or single-crystal samples [1,2]. A recent neutron diffraction study claims that $FeGa_3$ is magnetic with an ordering temperature above RT [9], potentially rendering it an interesting magnetic semiconductor.

External pressure provides a useful means to modify the hybridization strength between Fe $3d$ and Ga $4p$ states and to gauge the effect of such hybridization tuning on the physical properties, without introducing any chemical perturbation [6]. Pressurization thus serves as a parallel to extensive chemical doping studies performed on $FeGa_3$ [9–12], to cite a few cases which show the thermoelectric figure of merit ZT may be improved [13,14], itinerant antiferromagnetism occurs [11], or a ferromagnetic quantum critical point is induced [10].

Osorio-Guillén *et al.* [4] reported comprehensive density functional theory with additional on-site Hubbard corrections (DFT+U) studies, both on whether a magnetic ground state occurs in $FeGa_3$ at ambient pressure and on evolution of the band structure at high pressure. They also indicate $FeGa_3$ has a moderate electronic correlation strength (on-site repulsion to bandwidth ratio $U/W \sim 0.6$, U of 3–4 eV) and conclude that a nonmagnetic ground state is stabilized at ambient pressure. Their results show a gap closure and metallization ensue at ∼25 GPa due to a strong rearrangement of Fe $3d$ and Ga $4p$ hybridization near the Fermi level. Motivated by these previous results, we use an arsenal of probes to investigate the pressure response of $FeGa_3$ up to 30–35 GPa in diamond anvil cells (DACs). These include both resistivity measurements and ^{57}Fe Mössbauer spectroscopy (MS) at variable temperatures (300–3 K), as well as synchrotron x-ray diffraction (XRD) and x-ray absorption spectroscopy (XAS) at the Ga K edge both at RT. Methodological details are provided in the Supplemental Material [15–19].

Crystal structure considerations. $FeGa_3$ crystallizes in the tetragonal space group $P4_2/mnm$ (136) with $Z = 4$. Crystal structure renditions are available in Sec. S2 of the Supplemental Material [15]. Fe atoms occupy the $4f$ Wyckoff position and form dimerlike pairs along the [110] direction in the $z = 0$ plane and [1$\bar{1}$0] direction in the $z = 1/2$ plane. Note that first-principles calculations [5] do not show an appreciable charge density between Fe atoms in the dimer. Ga2- and Ga1-designated atoms occupy low-symmetry $8j$ and $4c$ Wyckoff positions, respectively. Eight Ga sites constitute the local environment around each Fe location in a bicapped-trigonal-prism (BTP) arrangement [20]. Ga2 atoms form the trigonal prism and Ga1 atoms are bounded to Fe by penetrating the prism faces.

*grhearne@uj.ac.za

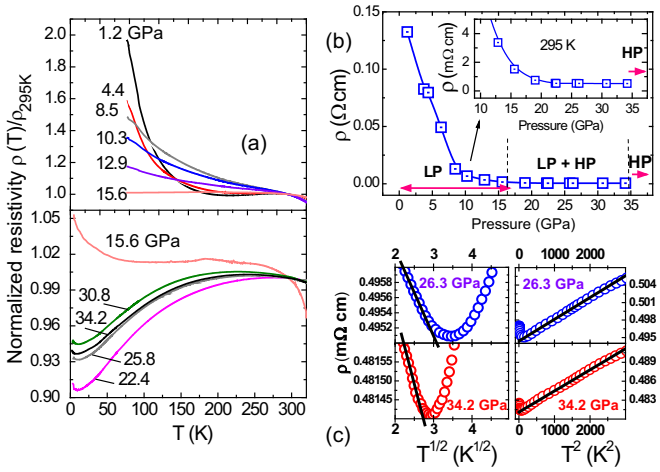

FIG. 1. (a) Plots of normalized resistivity for representative pressures of the low-pressure (LP) crystalline semiconducting phase (top panel) and metallic high-pressure (HP) phase (bottom panel). (b) Pressure evolution of resistivity at RT. (c) Linearized plots of low-temperature resistivity data of the HP phase, exemplifying the $T^{1/2}$ dependence below the resistivity minimum at $T<12$ K and Fermi-liquid T^2 dependence for 15–55 K.

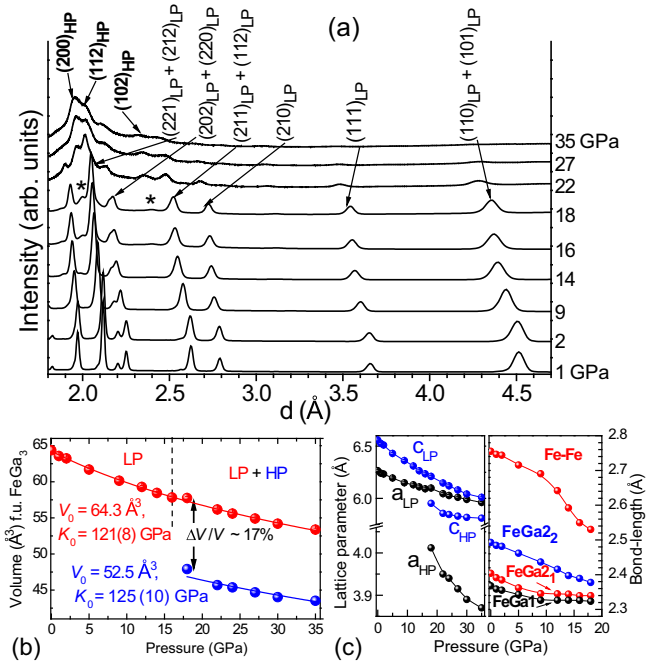

FIG. 2. (a) Selected synchrotron powder XRD profiles of $FeGa_3$ at RT as a function of pressure. Asterisks show the emerging most intense unique reflections of the HP phase beyond the onset pressure of 14–16 GPa. Characteristic tetragonal diffraction peaks of LP and HP phases are labeled. (b) Unit-cell volume vs pressure for both LP [$P4_2/mnm$ (136)] and HP [$P4_2/mmc$ (131)] phases. Solid circles are experimental data and fitted lines represent the third-order Birch-Murnaghan equation of state to obtain zero pressure volume V_0 and bulk modulus K_0 [59–61]. (c) Variation of lattice parameters (a and c) with pressure for LP and HP phases. The new HP phase initiates at 14–16 GPa and a coexisting remnant crystalline LP phase occurs with decreasing abundance up to 30–35 GPa. The right panel has the pressure variation of bond lengths for the LP tetragonal phase. Solid lines through data guide the eye. Error bars in (b) and (c) are the size of the symbols.

Results and discussion. The temperature dependence of the normalized electrical resistivity $\rho(T)$ in the range 1.2–13 GPa presented in Fig. 1(a) shows semiconducting behavior. At 15–16 GPa there is a particularly weak temperature dependence and near plateau behavior throughout most of the temperature range. At the next measured pressure increment to ~22 GPa, a distinctive positive temperature coefficient of resistivity (TCR) typical of metallic behavior occurs throughout most of the low-temperature range from 150 K down to ~12 K at which a minimum occurs. The resistivity develops a particularly weak temperature dependence above 150 K and exhibits a broad maximum in the vicinity of ~250 K. The low-temperature minimum and pressure-dependent broad high-temperature maximum occurring up to the highest-pressure measurement at ~34 GPa are deviations from the typical behavior of good metals [21]. A higher density of pressure points of the RT resistivity, ρ(295 K) in Fig. 1(b), confirms the semiconductor-metal transition seen in Fig. 1(a). Figure 1(b) (inset) shows an appreciable change to much lower pressure dependences of ρ(295 K) at ~15 GPa and a plateau behavior of ~0.5 mΩ cm above 25 GPa. These high ρ values and distinctive nonlinear behavior at high temperatures are indications of the onset of a "bad-metal" phase in the range 15–20 GPa. This contradicts a previous claim of a semiconductor-metal transition at a much lower pressure $P < 5$ GPa [22], based on resistance versus pressure measurements restricted to RT.

To ascertain how the semiconductor-metal transition relates to the structural/lattice response of the compound, diffraction data were measured up to ~35 GPa [see Fig. 2(a)] [23–26]. Typical reflections of the tetragonal $P4_2/mnm$ (136) phase are readily identified up to ~18 GPa. At 14–16 GPa new reflections develop at d values [marked with asterisks in Fig. 2(a)], in conjunction with original reflections of the low-pressure (LP) phase. These emergent features grow in intensity with increasing pressure. New reflections and other associated reflections overlapping with original reflections of the LP phase are a manifestation of the onset of a new high-pressure (HP) phase at 14–16 GPa, where a change to metallic behavior is triggered (see Fig. 1). A considerable diminution of LP reflections occurs at pressures above ~22 GPa and patterns become dominated by HP phase reflections at d values in the vicinity of 2.0 Å. The new HP phase can be indexed with space group $P4_2/mmc$ (131), a supergroup symmetry of the $P4_2/mnm$ (136) LP phase. The relation between unit-cell parameters of these two phases are $a_{LP} \sim \sqrt{2}(a_{HP})$ and $c_{LP} \sim c_{HP}$.

Structural parameters derived from refinements of XRD patterns are shown in Figs. 2(b) and 2(c) [23]. The derived unit-cell parameters reveal the emergent HP phase at 14–16 GPa has an unusually pronounced volume densification $\delta V/V \sim -17\%$ and similar compressibility compared with the LP phase. A two-phase Rietveld refinement involving $P4_2/mnm$ (136) and $P4_2/mmc$ (131) combinations is used to estimate phase fractions. After the onset of the HP phase at 16–18 GPa, its abundance evolves to 50% at 22 GPa and is ~80% at 27 GPa, at the expense of the LP phase. By further extrapolation we estimate a full conversion to the HP phase occurs just beyond ~35 GPa.

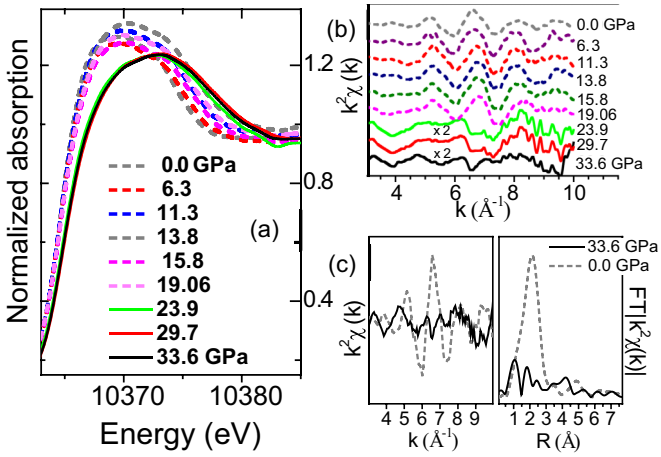

FIG. 3. Ga K-edge XAS data at RT. (a) Zoom over main XANES features demonstrating that data fall into two groups, LP related at $P<19$ GPa and HP related above this. (b) Associated k^2-weighted EXAFS of the LP phase and HP phase (scaled×2). (c) Fourier-transform magnitudes of k^2-weighted EXAFS at both starting and highest pressures, representing LP and HP phases, respectively.

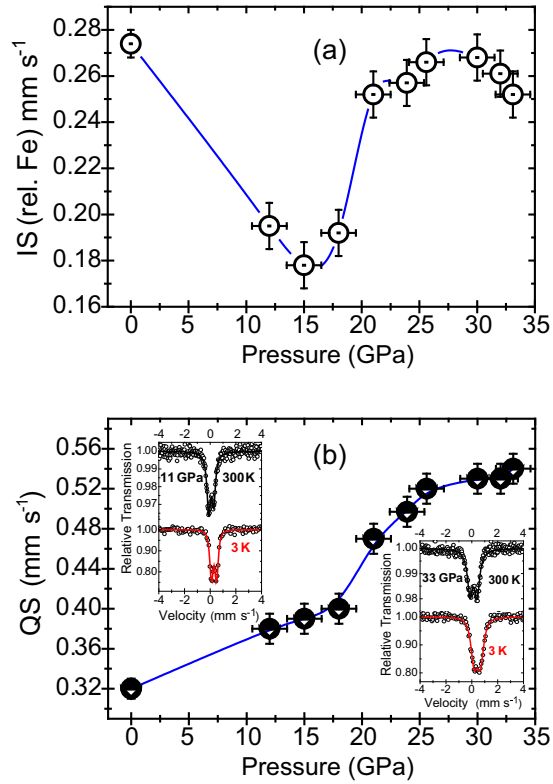

FIG. 4. Pressure dependence at RT of (a) isomer (centroid) shift IS and (b) QS (surrounding charge asphericity) parameters from doublet fits to ^{57}Fe Mössbauer spectra. Examples are shown as insets for LP and HP phases in the bottom panel [35]. Solid lines through data symbols in the main panels guide the eye. Note the onset of precipitous changes in the range 15–17 GPa, as described in the text.

The above-mentioned structural detail was not discerned in a previous pressure study of $FeGa_3$ by Mondal *et al.* [22], because of the excessive pressure marker contributions dominating their XRD patterns. They observed a severe diminution of LP phase reflections beyond 18 GPa and interpreted this as amorphization. However, they also noted the reappearance of strong reflections from the LP tetragonal phase upon decompression to ambient conditions from ∼33 GPa, similar to our findings.

Figure 2(c) also shows a pressure variation of bond lengths derived from Rietveld refinements of the data in Fig. 2(a). Compared to other bond lengths, the decrease in Fe-Fe distances develops a much stronger pressure dependence beyond ∼10 GPa. Osorio-Guillén *et al.* [4] used DFT+U-based computational studies of the $P4_2/mnm$ phase to contend that when Fe-Ga2 bond lengths become smaller than Fe-Ga1 bond lengths, a strong change in hybridization between Fe $3d$ and Ga $4p$ orbitals occurs near the Fermi level, leading to band-gap closure. This is predicted to occur at ∼25 GPa, with no suggestion of a structural transition (instability) occurring. These predictions are somewhat incompatible with our experimental findings. Figure 2(c) shows that a crossover of bond lengths does not occur up to 18 GPa, yet the onset of metallization is already occurring. Rather, metallization initiates concurrently with the emergence of the new HP phase in the range 14–16 GPa and is likely a consequence of this structural change.

An LP→HP structural change is corroborated by local probe experiments to high pressures involving Ga K-edge XAS [27–31] (see Fig. 3) and ^{57}Fe MS measurements [32–34] (see Fig. 4). Up to ∼19 GPa there is a continuous evolution of near-edge (XANES) features, followed by a distinct change above this pressure where a second group of XANES profiles may be distinguished. Compared with the LP suite, HP profiles at $P>19$ GPa are characterized by a clear shift in edge position, reduction in intensity, and broadening of the main XANES feature at ∼10370 eV [see Fig. 3(a)].

Figures 3(b) and 3(c) also demonstrate stark changes occurring in extended absorption fine structure (EXAFS) beyond 19 GPa. There is also a pronounced damping of the amplitudes. A comparison of the Fourier-transform magnitudes $\mathrm{FT}|k^2\chi(k)|$ of representative LP and HP EXAFS in Fig. 3(c) further highlights the change in the first-shell region $R\sim 2$ Å, suggestive of distinct Ga local environments for LP and HP phases.

The pressure evolution of the Fe local environment is tracked by the hyperfine interaction parameters from ^{57}Fe MS, derived from fitted quadrupole split (QS) spectral doublets (see Fig. 4) [35–39]. The isomer (centroid) shift (IS) at RT shows a monotonic decrease from ∼0.27 mm s^{-1} at ambient pressure to ∼0.18 mm s^{-1} at ∼15 GPa. This is anticipated when the s-electron density $|\psi_s(0)|^2$ increases at the Fe nucleus under compression because $\mathrm{IS}=-(\mathrm{constant})|\psi_s(0)|^2+(\mathrm{constant}')$, where the constants are atomic and nuclear parameters [40]. Beyond 15 GPa an unusual steep rise in IS occurs to a plateau at ∼0.26 mm s^{-1} in the range 20–25 GPa, after which there is a monotonic decrease expected with increasing densification beyond ∼27 GPa. Such a steep increase in IS is compatible with a change to a higher atomic coordination around the Fe probe [41,42]. Therefore, the onset of a phase transition at ∼15 GPa and evolution to a fully stabilized HP phase beyond ∼35 GPa involves a change to a higher than eightfold Ga coordination around the Fe sites. The aspheric electronic and lattice charge distribution around the Fe probe parametrized by

QS also exhibits an appreciable change in pressure dependence at ∼17 GPa, after which it increases monotonically to plateau values near ∼30 GPa. This is further corroboration of the BTP local environment changing to a more asymmetric environment for Fe atoms in the HP phase.

The changes in IS and QS parameters at the LP → HP transition, although conspicuous, are not typical of electronic spin crossover effects [40], normally also associated with an appreciable volume reduction [43,44]. If spin crossover was involved, then the IS would exhibit a relatively steep decrease and the QS a much larger change, associated with a redistribution of charge in 3*d* orbitals from electron spin pairing [40,45,46]. Thus steep changes in IS and QS in Fig. 4 are best ascribed to a concurrence of charge delocalization and increase in local coordination around the Fe sites. Moreover, only a quadrupole split doublet is discerned down to 3 K. The absence of a magnetic hyperfine structure suggests magnetic ordering (i.e., spin polarization) does not occur in both LP and HP phases.

Using the preceding elucidation of the structural/lattice evolution to 30–35 GPa, we attempt to account for radical deviations of the HP phase from the typical behavior of a good metal, notably the low-temperature resistivity minimum and high $\rho \sim 0.52$ mΩ cm values at RT. First, alloys having appreciable degrees of structural and compositional disorder exhibit a minimum in the resistivity at low temperatures [47,48]. This behavior is derived in part from enhanced electron-electron interaction effects associated with small electron mean free paths due to disorder-induced scattering [49–51]. Consequently, a temperature-dependent Aronov-Altshuler quantum correction needs to be added to the residual conductivity $\sigma_0 = 1/\rho_0$ for such diffusive electron motion. Hence the resistivity at temperatures below its minimum behaves as $\rho(T) = \rho_0(1 - \sigma_0^{-1} C T^{1/2})$ to lowest order, where C involves a combination of fundamental constants, diffusion constant D, and a screening parameter F [50,52,53]. Motivated by combined XRD, XAS, and MS indications of appreciable atomic rearrangements at the LP→HP transition in $FeGa_3$, we have checked our low-temperature resistivity data for such a $\rho(T)$ vs $T^{1/2}$ correlation found in many disordered alloys [48,54]. Definitive $T^{1/2}$ behavior indeed occurs in the range 4–9 K, as shown in Fig. 1(c). At higher temperatures 15–50 K, distinct T^2 Fermi-liquid behavior ensues from various inelastic scattering mechanisms.

Second, the high $\rho \sim 0.52$ mΩ cm at RT and broad maximum discerned at high temperatures in Fig. 1(a) is corroboration of suggested disorder in the HP metallic state. This level of resistivity corresponds to an electron mean free path of $l \sim 4$ Å, similar to the interatomic spacing and typical of diffusive motion in amorphous and disordered alloys where a low-temperature resistivity minimum also occurs [55]. Tsuei [56] also showed that in disordered metals there is a critical resistivity ρ_c where crossover occurs from a positive to negative TCR over an extended temperature range. This depends separately on material properties characterized by the k_F Fermi-level wave vector and on the degree of disorder reflected in restricted values for l [56]. The broad maximum in ρ at high temperatures signifies that the HP phase of $FeGa_3$ is on the verge of this TCR crossover. Using the formulation of Tsuei [56] involving $\rho_c \sim 0.5$ mΩ cm and the estimated $l \sim 4$ Å, it is deduced that $k_F \leqslant 1.0$ Å^{-1} [57,58], corresponding to a low carrier density system.

Concluding summary. $FeGa_3$ transitions to a new HP phase, with an onset at 14–16 GPa, and a pronounced ∼17% volume collapse. A crystalline LP tetragonal phase, $P4_2/mnm$ (136), coexists in progressively decreasing abundance with the new HP phase having the $P4_2/mmc$ (131) supergroup crystal symmetry. Our XRD results suggest that a full conversion to the HP phase occurs just beyond ∼35 GPa. The Ga *K*-edge XAS and Fe MS local probes indicate significant atomic rearrangements occur at the LP → HP structural transition.

The onset of metallic behavior occurs in the range 16–20 GPa, concurrent with the initiation of the LP→HP structural transition. The HP phase exhibits a resistivity minimum at 8–12 K, below which there is a $T^{1/2}$ dependence typical of enhanced electron-electron interaction effects from diffusive motion in disordered metallic alloys. The weak high-temperature dependence of the resistivity manifestation as a broad maximum and high $\rho \sim 0.5$ mΩ cm at RT infers the high-density HP phase to be a disordered metallic alloy (small electron mean free path of ∼4 Å) of low carrier density (Fermi wave vector $k_F < 1$ Å^{-1}) on the verge of an Anderson transition.

This high-density disordered "bad metal" reverts to the original $P4_2/mnm$ (136) crystalline structure upon decompression from ∼35 GPa to ambient conditions. To enable this back-transformation, some form of "memory" of the original lattice network, e.g., Fe-Fe dimers, may have been retained in the LP→HP structural transformation to a denser metallic state.

Acknowledgments. G.R.H., E.C., and S.B. acknowledge financial support from the National Research Foundation of South Africa (Grants No. 105870 and No. 90698, and for a postdoctoral research fellowship award). Research funding for this project from the URC of the University of Johannesburg is also acknowledged with gratitude. B.J. acknowledges IISc Bangalore and ICTP Trieste for financial support through the award of the IISc-ICTP fellowship. We also thank various beamline scientists at the ID-24 and ID-18 beamlines of the ESRF for assistance with the XAS and nuclear resonance spectroscopy measurements, respectively. Dr Narcizo Souza-Neto of the Brazilian Synchrotron Light Laboratory (LNLS) is acknowledged with gratitude for insightful observations on the XAS and XRD data.

[1] M. Wagner-Reetz, D. Kasinathan, W. Schnelle, R. Cardoso-Gil, H. Rosner, and Y. Grin, Phys. Rev. B **90**, 195206 (2014).
[2] U. Häussermann, M. Boström, P. Viklund, Ö. Rapp, and T. Björnängen, J. Solid State Chem. **165**, 94 (2002).
[3] Z. P. Yin and W. E. Pickett, Phys. Rev. B **82**, 155202 (2010).
[4] J. M. Osorio-Guillén, Y. D. Larrauri-Pizarro, and G. M. Dalpian, Phys. Rev. B **86**, 235202 (2012).
[5] A. S. Botana, Y. Quan, and W. E. Pickett, Phys. Rev. B **92**, 155134 (2015).
[6] P. S. Riseborough, Adv. Phys. **49**, 257 (2000).
[7] Z. Schlesinger, Z. Fisk, H.-T. Zhang, and M. B. Maple, Physica B **237-238**, 460 (1997).
[8] J. M. Tomczak, K. Haule, and G. Kotliar, Proc. Natl. Acad. Sci. U.S.A. **109**, 3243 (2012).

[9] M. B. Gamża, J. M. Tomczak, C. Brown, A. Puri, G. Kotliar, and M. C. Aronson, Phys. Rev. B **89**, 195102 (2014).

[10] K. Umeo, Y. Hadano, S. Narazu, T. Onimaru, M. A. Avila, and T. Takabatake, Phys. Rev. B **86**, 144421 (2012).

[11] A. A. Gippius, V. Y. Verchenko, A. V. Tkachev, N. E. Gervits, C. S. Lue, A. A. Tsirlin, N. Büttgen, W. Krätschmer, M. Baenitz, M. Shatruk *et al.*, Phys. Rev. B **89**, 104426 (2014).

[12] E. M. Bittar, C. Capan, G. Seyfarth, P. G. Pagliuso, and Z. Fisk, J. Phys.: Conf. Ser. **200**, 012014 (2010).

[13] N. Haldolaarachchige, A. B. Karki, W. A. Phelan, Y. M. Xiong, R. Jin, J. Y. Chan, S. Stadler, and D. P. Young, J. Appl. Phys. **109**, 103712 (2011).

[14] Y. Takagiwa, Y. Matsuura, and K. Kimura, J. Electron. Mater. **43**, 2206 (2014).

[15] See Supplemental Material at http://link.aps.org/supplemental/10.1103/PhysRevB.98.020101, which also includes details on sample synthesis and characterization involving Ref. [16], pressure determination by means of ruby fluorescence calibration [17], and comments on the effect of nonhydrostaticity in the latter part of Sec. S6 which involve Refs. [18,19].

[16] N. Tsujii, H. Yamaoka, M. Matsunami, R. Eguchi, Y. Ishida, Y. Senba, H. Ohashi, S. Shin, T. Furubayashi, and H. Abe, J. Phys. Soc. Jpn. **77**, 024705 (2008).

[17] A. D. Chijioke, W. J. Nellis, A. Soldatov, and I. F. Silvera, J. Appl. Phys. **98**, 114905 (2005).

[18] S. Klotz, J. C. Chervin, P. Munsch, and G. L. Marchand, J. Phys. D: Appl. Phys. **42**, 075413 (2009).

[19] A. Dewaele, F. Datchi, P. Loubeyre, and M. Mezouar, Phys. Rev. B **77**, 094106 (2008).

[20] J. K. Burdett, R. Hoffmann, and R. C. Fay, Inorg. Chem. **17**, 2553 (1978).

[21] O. Gunnarsson, M. Calandra, and J. E. Han, Rev. Mod. Phys. **75**, 1085 (2003).

[22] D. Mondal, V. Srihari, C. Kamal, H. Poswal, A. B. Garg, A. Thamizhavel, S. Banik, A. Chakrabarti, T. Ganguli, and S. M. Sharma, Phys. Rev. B **95**, 134105 (2017).

[23] See Sec. S4 of Supplemental Material [15] for details of the XRD data reduction and analyses, which includes Refs. [24–26].

[24] A. P. Hammersley, ESRF Internal Report No. ESRF97HA02T, 1997 (unpublished), http://www.esrf.eu/computing/scientific/FIT2D/.

[25] A. P. Hammersley, S. O. Svensson, M. Hanfland, A. N. Fitch, and D. Hausermann. High Press. Res. **14**, 235 (1996).

[26] J. Rodriguez-Carvajal, FULLPROF: A Program for Rietveld Refinement and Pattern Matching Analysis, https://www.ill.eu/sites/fullprof/.

[27] See Sec. S5 of Supplemental Material [15] for details of the XAS data analyses, which includes Refs. [28–31].

[28] S. Pascarelli, O. Mathon, T. Mairs, I. Kantor, G. Agostini, C. Strohm, S. Pasternak, F. Perrin, G. Berruyer, P. Chappelet *et al.*, J. Synchrotron Radiat. **23**, 353 (2016).

[29] E. Paris, B. Joseph, A. Iadecola, C. Marini, H. Ishii, K. Kudo, S. Pascarelli, M. Nohara, T. Mizokawa, and N. L. Saini, Phys. Rev. B **93**, 134109 (2016).

[30] B. Joseph, R. Torchio, T. I. C. Benndorf, T. Shinmei, R. Pöttgen, and A. Zerr, Phys. Chem. Chem. Phys. **19**, 17526 (2017).

[31] B. Joseph, A. Iadecola, B. Schiavo, A. Cognigni, L. Olivi, G. D'Alì Staiti, and N. L. Saini, J. Solid State Chem. **183**, 1550 (2010).

[32] G. R. Hearne, M. P. Pasternak, and R. D. Taylor, Rev. Sci. Instrum. **65**, 3787 (1994).

[33] G. Yu. Machavariani, M. P. Pasternak, G. R. Hearne, and G. Kh. Rozenberg, Rev. Sci. Instrum. **69**, 1423 (1998).

[34] V. Potapkin, A. I. Chumakov, G. V. Smirnov, J.-P. Celse, R. Rüffer, C. McCammon, and L. Dubrovinsky, J. Synchrotron Rad. **19**, 559 (2012).

[35] See Sec. S6 of Supplemental Material [15] for details of ^{57}Fe MS data analyses, which includes Refs. [36–39].

[36] R. A. Brand, WinNormos-for-Igor, Universität-GH-Duisburg and distributed by Wissenschaftliche Elektronik GmbH, http://www.wissel-instruments.de.

[37] Z. Klencsár, MossWinn 4.0, http://www.mosswinn.com/.

[38] C. Prescher, MossA, http://www.clemensprescher.com/.

[39] C. Prescher, C. McCammon, and L. Dubrovinsky, J. Appl. Crystallogr. **45**, 329 (2012).

[40] P. Gütlich, E. Bill, and A. X. Trautwein, *Mössbauer Spectroscopy and Transition Metal Chemistry: Fundamentals and Applications* (Springer, Berlin, 2011).

[41] R. Greatrex and N. N. Greenwood, Discuss. Faraday Soc. **47**, 126 (1969).

[42] M. Darby Dyar, D. G. Agresti, M. W. Schaefer, C. A. Grant, and E. C. Sklute, Annu. Rev. Earth Planet. Sci. **34**, 83 (2006).

[43] Y. Wang, Z. Zhou, T. Wen, Y. Zhou, N. Li, F. Han, Y. Xiao, P. Chow, J. Sun, M. Pravica *et al.*, J. Am. Chem. Soc. **138**, 15751 (2016).

[44] Y. Wang, L. Bai, T. Wen, L. Yang, H. Gou, Y. Xia, P. Chow, M. Pravica, W. Yang, and Y. Zhao, Angew. Chem. Int. Ed. **55**, 10350 (2016).

[45] W. M. Xu, G. R. Hearne, S. Layek, D. Levy, J.-P. Itié, M. P. Pasternak, G. K. Rozenberg, and E. Greenberg, Phys. Rev. B **96**, 045108 (2017).

[46] J.-F. Lin, S. Speziale, Z. Mao, and H. Marquardt, Rev. Geophys. **51**, 244 (2013).

[47] O. Rapp, S. M. Bhagat, and H. Gudmundsoon, Solid State Commun. **42**, 741 (1982).

[48] T. K. Nath and A. K. Majumdar. Phys. Rev. B **55**, 5554 (1997).

[49] J. S. Dugdale, Contemp. Phys. **28**, 547 (1987).

[50] M. A. Howson and B. L. Gallagher, Phys. Rep. **170**, 265 (1988).

[51] J. F. DiTusa, K. Friemelt, E. Bucher, G. Aeppli, and A. P. Ramirez, Phys. Rev. B **58**, 10288 (1998).

[52] P. A. Lee and T. V. Ramakrishnan, Rev. Mod. Phys. **57**, 287 (1985).

[53] W. Dyckhoff, G. Fritsch, and E. Lühscher, J. Phys. Chem. **94**, 1123 (1990).

[54] U. Mizutani, Mater. Sci. Eng. **99**, 165 (1988).

[55] U. Mizutani, *Introduction to the Electron Theory of Metals* (Cambridge University Press, Cambridge, U.K., 2001).

[56] C. C. Tsuei, Phys. Rev. Lett. **57**, 1943 (1986).

[57] See Sec. S3.2 of Supplemental Material [15] for further details of these analyses, which includes Ref. [58].

[58] J. H. Mooij, Phys. Status Solidi A **17**, 521 (1973).

[59] See the latter part of Sec. S4.2 of Supplemental Material [15] for details of the equation of state analyses, which includes Refs. [60,61].

[60] F. Birch, J. Geophys. Res. **83**, 1257 (1978).

[61] R. J. Angel, J. Gonzalez-Platas, and M. Alvaro, Z. Kristallogr. **229**, 405 (2014).